Available online at www.sciencedirect.com
ScienceDirect
Trans. Nonferrous Met. Soc. China 31(2021) 207−221
Transactions of Nonferrous Metals Society of China
www.tnmsc.cn

Oxidation and hot corrosion behaviors of Nb−Si based ultrahigh temperature alloys at 900 °C

Jia-hua HE, Xi-ping GUO, Yan-qiang QIAO

State Key Laboratory of Solidification Processing, Northwestern Polytechnical University, Xi'an 710072, China

Received 19 February 2020; accepted 30 July 2020

Abstract: Oxidation and hot corrosion behaviors at 900 °C of Nb−Si based ultrahigh temperature alloys were investigated. Both oxidation and hot corrosion kinetics curves of the alloy involve an initial parabolic stage and a later rapid linear stage. In the initial oxidation stage (1−50 h), a thin and continuous scale is formed on the alloy surface, while severe pest degradation phenomenon is observed in the linear oxidation stage. Compared with oxidation of the alloy in static air, a linear hot corrosion stage happens earlier and catastrophic scale disintegration occurs after hot corrosion for 20−100 h, demonstrating that molten salts (Na_2SO_4 and NaCl) could significantly accelerate the oxidation process of the alloy. STEM results indicate that the corroded scale consists mainly of TiO_2, Nb_2O_5, $TiNb_2O_7$, amorphous silicate and $NaNbO_3$.

Key words: Nb−Si based alloys; molten salts; oxidation; hot corrosion; silicate

1 Introduction

The need for high performance structural materials in aerospace and industrial components operating at high temperatures has led to a surge in the development of refractory metal silicide based intermetallics, multiphase alloys and composites. Nb−Si based alloys are prospective candidates for high-temperature structural applications due to their low densities (6.6−7.2 g/cm^3), high melting points (over 1750 °C) and excellent high temperature strength and creep performance [1,2]. In recent years, multi-alloying of Nb−Si based alloys has been developed to achieve an excellent balance among high temperature strength, room temperature fracture toughness and oxidation resistance [3,4]. The microstructure of these alloys consists of niobium solid solution (Nbss) and brittle intermetallics phases such as α, β, $\gamma(Nb,X)_5Si_3$, $(Nb,X)_3Si$ and $(Cr,X)_2Nb$ Laves phases ("X" represents Ti, Hf, Al, etc). To date, multi-component Nb−Si based ultrahigh temperature alloys display compressive strengths as high as 550 MPa at 1200 °C, 450 MPa at 1300 °C and 200 MPa at 1500 °C [5]. Room temperature fracture toughness (K_Q) of these alloys has been reported over 20 MPa·m$^{1/2}$ through composition optimization and directional solidification [6,7]. In consequence, Nb−Si based ultrahigh temperature alloys are promising candidates for future turbine-engine applications due to possessing favorable mechanical properties at high and room temperature.

Numerous essential engineering systems (e.g. aircraft engines and industrial gas turbines) operating at high temperatures involve contact of metallic materials or components with combustion product gases or other oxidizing gases. These metallic materials or components suffer from a salt deposit-induced (e.g. Na_2SO_4, NaCl and $NaVO_3$) accelerated oxidation, i.e. hot corrosion [8,9]. Among these salts, Na_2SO_4 is the main salt in high-temperature hot corrosion process, which is resulted from the salt ingested into the engine and

Corresponding author: Xi-ping GUO; Tel/Fax: +86-29-88494873; E-mail: xpguo@nwpu.edu.cn
DOI: 10.1016/S1003-6326(20)65488-7

sulfur from the combustion of fuel. Chloride contaminants are difficult to remove from the fuel source and it may be present in the environment, especially in the marine environment [10]. Until now, many investigations have been focused on hot corrosion behavior of Ti−Al based alloys, Co-based alloys, Ni-based superalloys and their protective coatings [11−13]. Nevertheless, hot corrosion mechanism induced by Na_2SO_4 and NaCl molten salts of Nb−Si based ultrahigh temperature alloys has not been studied extensively [14]. In addition, oxidation mechanism of Nb−Si based alloys at intermediate temperature (900 °C) has not been understood clearly and whether "pest" phenomenon would occur deserves to be studied deeply [15,16]. Therefore, the motivation for this work is to investigate the hot corrosion and intermediate temperature oxidation behaviors of Nb−Si based alloys. Furthermore, the hot corrosion mechanism is discussed as well.

2 Experimental

The Nb−Si based ultrahigh temperature alloy ingot (Nb−22Ti−15Si−5Cr−3Al−2.5Hf (at.%)) was fabricated through high frequency induction melting. In order to obtain an equilibrium microstructure, the as-cast alloy ingot was annealed at 1450 °C for 50 h in a high vacuum heat-treatment furnace. After heat-treatment, the ingot was cut into small cubes with the dimension of 7 mm × 7 mm × 7 mm by electro-discharge machining. All sides of the specimens were ground to 1200 grit SiC papers, then cleaned in an ultrasonic acetone bath and finally dried.

The oxidation and hot corrosion tests at 900 °C for the alloy were carried out in a muffle furnace. Before tests, all alumina crucibles were heated to 900 °C until no mass change was observed. Corrosion medium was the saturated aqueous solution of a mixture of Na_2SO_4 + NaCl (with a mass ratio of 3:1). Prior to the hot corrosion test, the specimen was preheated at 250 °C on a hot plate and then all the surfaces were coated with the mixed salts. Average salt supply is about 3 mg/cm^2. The specimen with mixed salts was placed into the alumina crucible and then was heated to 900 °C in a muffle furnace. In order to ensure adding the similar amount of salts, the specimens were taken out from the furnace after exposing a certain time, recoated by the salt and then taken to next cycle (the furnace time in one cycle is 10 h). The testing time was set as 1, 5, 10, 20, 50, 70 and 100 h. The detailed experiment process is also presented in our previous work [17].

The phase constituents of oxidized and hot corroded specimens were identified using X-ray diffraction analysis (XRD, Panalytical X'Pert PRO). A scanning electron microscope (SEM, TESCAN MIRA 3) equipped with an energy dispersive spectroscopy (EDS) was used to characterize the microstructure of the oxidized and hot corroded specimens. An electron probe micro-analyzer (EPMA−1720, SHIMADZU) with a wavelength dispersive spectrometer (WDS) was used to determine the composition and microstructure of the oxidation and corrosion products. A scanning/transmission electron microscope (STEM, Talos F200 X) equipped with a high-angle annular dark field (HAADF) detector and super X-EDS system was employed to identify constituent phases of corrosion products.

3 Result and discussion

3.1 Microstructure of bare alloy

Figure 1 displays the heat-treated microstructure of Nb−Si based ultrahigh temperature alloy. Table 1 gives the chemical compositions of the main phases. It can be seen that small and broken $(Nb,X)_5Si_3$ (X represents Ti, Cr, Hf, etc) blocks including α and γ phases are uniformly distributed in the Nbss matrix. EDS results reveal that the solid solubility of Hf, Ti and Al in γ phase is relatively high, while Cr element is mainly dissolved in Nbss.

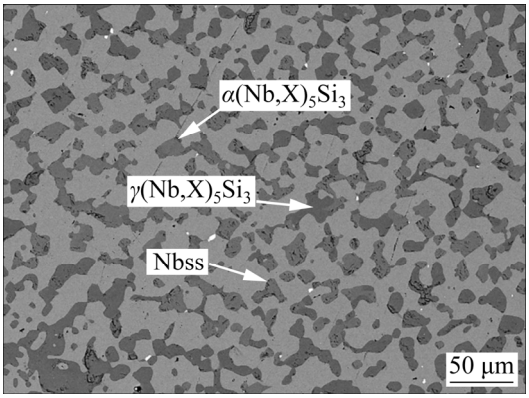

Fig. 1 Heat-treated microstructure of Nb−Si based alloys

Table 1 Chemical compositions of heat-treated Nb−Si based alloys analyzed by EDS

Phase	Composition/at.%					
	Nb	Ti	Si	Cr	Al	Hf
Nbss	65.0	22.1	1.3	6.6	3.8	1.2
$\alpha(Nb,X)_5Si_3$	50.7	13.6	33.0	0.3	0.4	2.0
$\gamma(Nb,X)_5Si_3$	39.6	18.8	35.4	0.6	2.3	3.3

3.2 Oxidation and hot corrosion kinetics curves

Oxidation and hot corrosion tests of Nb−Si based alloys were carried out at 900 °C. The corresponding kinetics curves and partial macrographic morphologies are presented in Fig. 2. At 900 °C, the oxidation process of the alloy could be divided into two main stages: an initial parabolic stage (0−50 h) followed by a rapid linear oxidation stage (over 50 h). The later linear oxidation kinetics indicates that the scale could not provide an effective barrier for oxygen ingress towards the alloy being exposed in the static air. Particularly, pest-like oxidation products (powdered and cracked scale) are observed on the alloy surface after 100 h exposure in air and the final mass gain is approximately 38 mg/cm^2. Nevertheless, not only a linear corrosion stage happens earlier (over 20 h), but also a drastic increase of mass gain (97 mg/cm^2) and severely catastrophic scale disintegration occur after hot corrosion for 100 h, demonstrating that the molten salts (Na_2SO_4 and NaCl) could significantly accelerate the oxidation process of Nb−Si based alloys. Figure 2(b) shows the fitting curves at the parabolic stages of oxidation and hot corrosion processes of Nb−Si based alloys. It can be seen that the parabolic hot corrosion rate constant is two orders of magnitude higher than the parabolic oxidation rate constant.

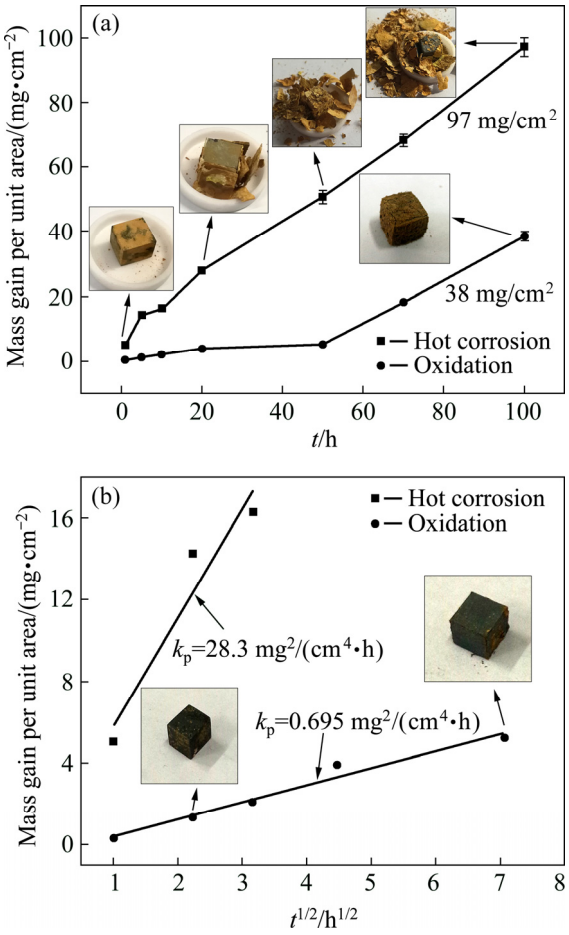

Fig. 2 Oxidation and hot corrosion kinetics curves at 900 °C of Nb−Si based alloys and their partial macrographic morphologies: (a) Comparisons of oxidation and hot corrosion kinetics curves; (b) Linear fitting curves for mass gain per unit area versus square root of time for oxidation and hot corrosion

3.3 Oxidation products

The oxidized products of Nb−Si based alloys are analyzed by X-ray diffractometer (Fig. 3). XRD patterns show that all the scales are composed of TiO_2 (JCPDS 76-0325, tetragonal) and Nb_2O_5 (JCPDS 72-1297, monoclinic). Compared to those with the substrate alloy, the diffraction peaks from Nbss are weakened substantially and TiO_2, Nb_2O_5 peaks are observed after 10 h of exposure in air, which is mainly responsible for the preferential oxidation of Nbss. Moreover, the diffraction peak intensity of the oxidation products (TiO_2 and Nb_2O_5) becomes stronger as the exposure time prolongs. Figures 4(a, b) show the surface morphologies of Nb−Si based alloys after oxidation for 10 h. The

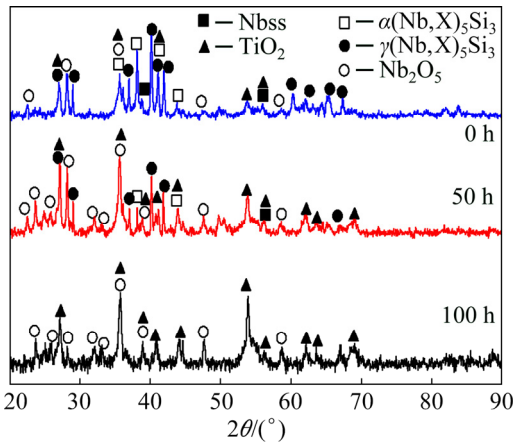

Fig. 3 XRD patterns conducted on surface of Nb−Si based alloys after oxidation at 900 °C

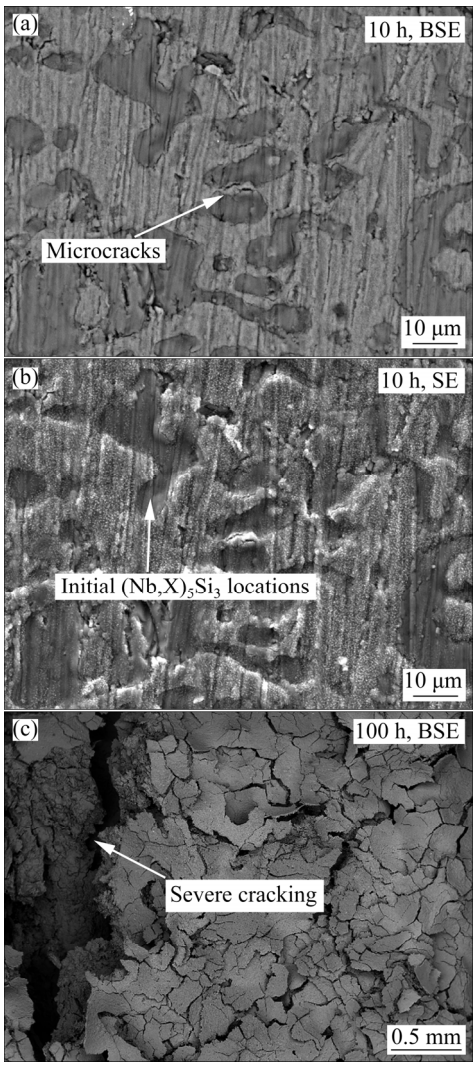

Fig. 4 Surface morphologies of Nb−Si based alloys after oxidation at 900 °C for 10 h (a, b) and 100 h (c)

specimen surface exhibits similar morphology characteristics to the substrate alloy, and SE image indicates that significant volume expansion occurs in the original Nbss, and then brings microcracks at the original Nbss/silicide interfaces. After oxidation for 100 h (Fig. 4(c)), the scale shows the tendency of severe scale cracking and disintegrating like "pesting".

Figure 5 represents the cross-sectional microstructures of Nb−Si based alloys after oxidation at 900 °C. A very thin (~2.7 μm), dense and continuous scale comprising light-gray phase and dark-gray phase is formed after oxidation for 10 h. The light-gray phase with some transverse microcracks consists of Nb (~17.51 at.%) and Ti (~6.50 at.%) mixed oxides. The dark-gray phase is identified as Si-rich oxide (~9.82 at.% Si), which is

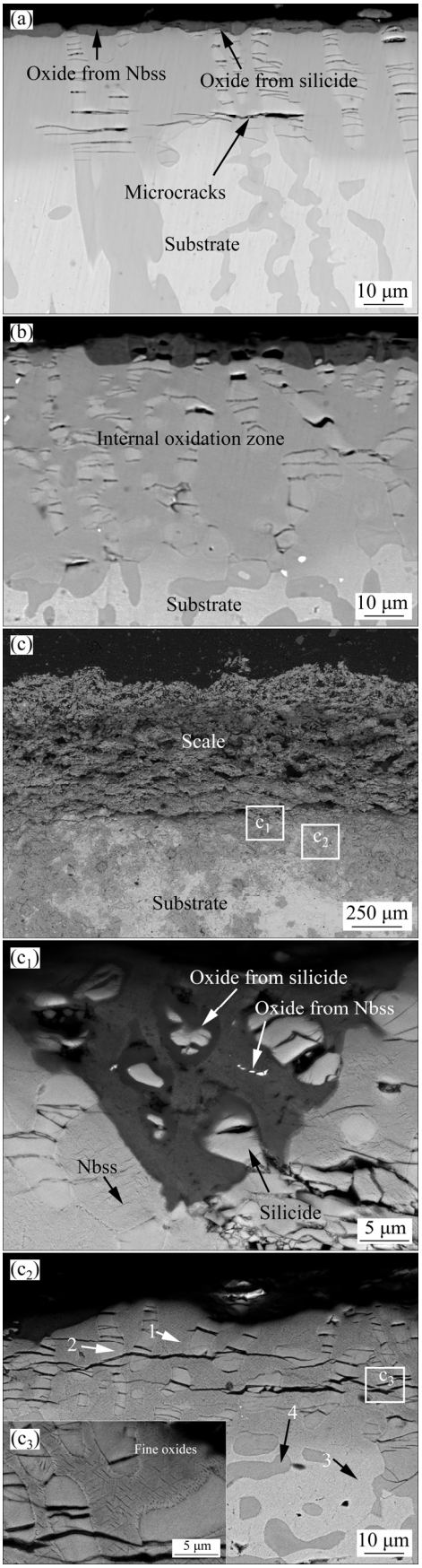

Fig. 5 Cross-sectional BSE images of Nb−Si based alloys after oxidation at 900 °C for 10 h (a), 50 h (b) and 100 h (c, c_1, c_2, c_3)

evolved from silicide. With subsequent increase in oxidation time (50 h), the oxide layer gradually thickens and some holes are observed in the Si-rich oxide, as shown in Fig. 5(b). Nevertheless, a loose, fragmentized and powdery scale with a thickness of about 650 μm is formed after exposure of 100 h in air (Fig. 5(c)), indicating that the alloy has experienced a unstable oxidation stage. Meanwhile, many horizontal cracks as well as holes are observed in the scale in the later linear oxidation stage. Figure 5(c_1) shows the BSE image of oxidized alloy at scale/substrate interface. Preferential oxidation of Nbss and partial oxidation of silicide blocks are found, suggesting that the oxidation process of the alloy is mainly controlled by inward diffusion of oxygen ions and oxygen intruding into silicide is much more difficult [16].

In addition, a separate layer marked as internal oxidation zone (IOZ) is observed between scale and substrate, as shown in Figs. 5(a, b, c_2). Oxygen intruding into Nbss leads to the formation of this layer, which is featured by dark-gray Nbss matrix (~26.12 at.% O) and cracked silicide blocks. After oxidation at 900 °C for 10 h, numerous cracks are observed in the silicide of IOZ and propagate parallel to scale/substrate interface. The width of these cracks increases gradually and microcrack initiation occurs at the silicide/Nbss interface after oxidation for 50 h (Fig. 5(b)). After oxidation for 100 h, these cracks cross silicide blocks and then extend into Nbss matrix along the Nbss/silicide interface, eventually resulting in penetrative cracking of IOZ (Fig. 5(c_2)). Table 2 presents the chemical compositions of marked sites in Fig. 5(c_2). WDS analysis results show that oxygen content in Nbss matrix (IOZ) is about 28.50 at.%, much higher than that in silicide blocks (~4.79 at.%). Moreover, massive needle-like oxides (TiO_2, Al_2O_3 and Cr_2O_3), marked by a white arrow in Fig. 5(c_3), are also found in the Nbss matrix. Formation of these fine oxides and oxygen dissolving into Nbss matrix could lead to volume expansion of Nbss, then induce initiation and propagation of cracks in silicides, and eventually accelerate the oxidation process of the alloy.

Table 2 Chemical compositions of marked sites in Fig. 5(c_2), determined by WDS analysis

Position	Composition/at.%						
	Nb	Ti	Si	Cr	Al	Hf	O
1	42.16	18.74	0.36	6.19	3.17	0.88	28.50
2	30.60	24.15	32.63	0.65	2.66	4.52	4.79
3	53.78	23.93	0.40	8.20	3.74	1.12	8.83
4	29.14	25.62	33.67	0.63	2.53	4.67	3.74

3.4 Hot corrosion products

Figure 6 presents the XRD patterns of hot corrosion products formed on Nb−Si based alloys. It is shown that the hot corrosion products for 1 h are mainly composed of Nb_2O_5, TiO_2 and monoclinic $NaNbO_3$ (JCPDS 74-2441). In addition, some diffraction peaks from complex products of $TiNb_2O_7$ (JCPDS 39-1407), $Na_2Nb_4O_{11}$ (JCPDS 44-0060) and $Na_2Nb_8O_{21}$ (JCPDS 13-0329) are also detected on the XRD patterns of the hot corrosion products for 20−100 h. No XRD peaks from Si-containing products are found, possibly due to the formation of amorphous silicate [17,18]. Figure 7 shows the surface morphologies of Nb−Si based alloys after hot corrosion for 1 and 20 h. The loose scale is characterized by some dark nubbles distributing on the gray matrix, as shown in Figs. 7(a, a_1). The EDS results reveal that the dark phase is TiO_2 with a composition of 3.8Nb−19.2Ti−0.6Si−2.4Cr−6.2Al−0.4Hf−0.1S−0.2Cl−3.0Na−64.1O (at.%), while the light gray matrix could be recognized as (Nb,Ti)-oxide, which has a composition of 13.2Nb−4.5Ti−1.7Si−4.0Cr−3.8Al−0.9Hf−0.1S−0.1Cl−3.0Na−68.7O (at.%). Some small dark-gray (Na,Nb)-oxide particles are also found in the scale. With prolonging exposure time to 20 h, not only the dark TiO_2 nubbles coarsen

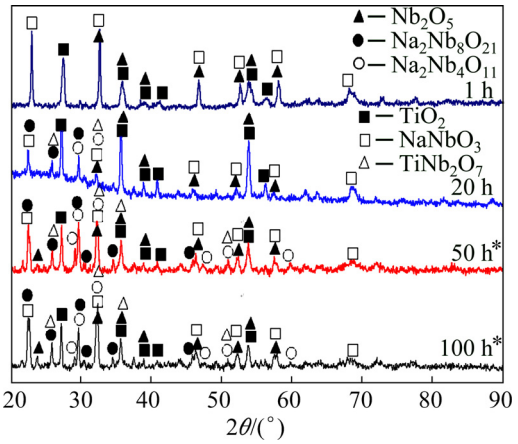

Fig. 6 XRD patterns of scale formed on Nb−Si based alloys after hot corrosion at 900 °C (* means that the peeling scale was ground into powders and then characterized by X-ray diffraction analysis)

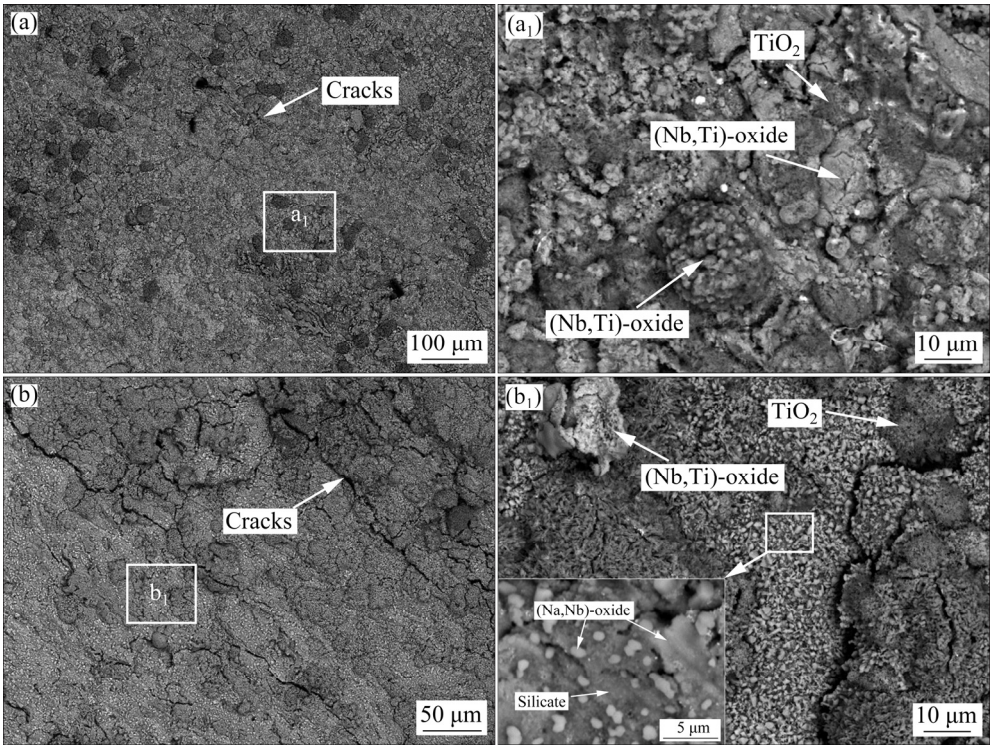

Fig. 7 Surface morphologies of Nb−Si based alloys after hot corrosion for 1 h (a, a_1) and 20 h (b, b_1)

but also the amount of (Na,Nb)-oxide particles increases. Besides, amorphous silicate is also observed underneath $NaNbO_3$ particles, as inserted in the lower left corner of Fig. 7(b_1). Moreover, serious cracking (Fig. 7(b)) and spallation (Fig. 2(a)) of scale occur after exposure in the molten salts.

Figure 8 represents the cross-sectional BSE images of Nb−Si based alloys after hot corrosion for 1 and 20 h. The corroded specimen is primarily composed of a loose, fragmentary scale and an internal oxidation zone. Combined with XRD patterns (Fig. 6) and WDS results (Table 3), it can be determined that all the loose and fractured scales mainly consist of Nb_2O_5, $TiNb_2O_7$, TiO_2, silicate and (Na,Nb)-oxide. However, Nb_2O_5 and $TiNb_2O_7$ cannot be easily distinguished by BSE and WDS analyses, due to their similar composition and contrast. At the lower part of the scales, some sporadic bright silicide patches are found in the dark-gray silicate blocks, demonstrating that silicide is harder to be corroded than Nbss. Figure 9 shows the XRD pattern and SEM images of the residual scale formed on Nb−Si based alloys after hot corrosion for 50 h. The XRD pattern of residual scale shows many strong $Na_2Nb_4O_{11}$ and $Na_2Nb_8O_{21}$ peaks in contrast with that of 20 h. Besides, the surface of residual scale appears to be much flatter upon exposure of 50 h. Dark-gray TiO_2 patches, numerous bright (Na,Nb)-oxide coacervates and light-gray silicate blocks co-exist on the surface (Fig. 9(c)). WDS analysis reveals that these bright coacervates have a composition with higher Nb content (18.52Nb−2.39Ti−0.14Si−1.28Cr−0.82Al−0.28Hf−0.20S−0.08Cl−10.51Na−65.88O, at.%) and the molar ratio of Nb to Na roughly approaches 1.8:1. Hence, it can be inferred that the bright phase is a sodium-niobate mixture of $NaNbO_3$, $Na_2Nb_4O_{11}$ and/or $Na_2Nb_8O_{21}$. With prolonging exposure time to 100 h, scale exfoliation occurs and then the substrate exhibits partly exposed, as shown in Figs. 2 and 10(b). The residual scale primarily consists of light-gray (Nb,Ti)-oxide, dark-gray lath-like silicate as well as some residual silicide patches (Figs. 10(c, d)). It is worth mentioning that beneath the broken scale there also exists an internal oxidation zone, which is characterized by dark-gray Nbss matrix and cracked silicide blocks (Figs. 8, 9 and 10).

Figure 11 shows elemental mapping of internal oxidation zone of Nb−Si based alloys after hot corrosion for 20 h (EPMA). Na mainly exists in the form of sodium-niobate in the scale, while a small quantity of sulfur and chlorine is detected in the

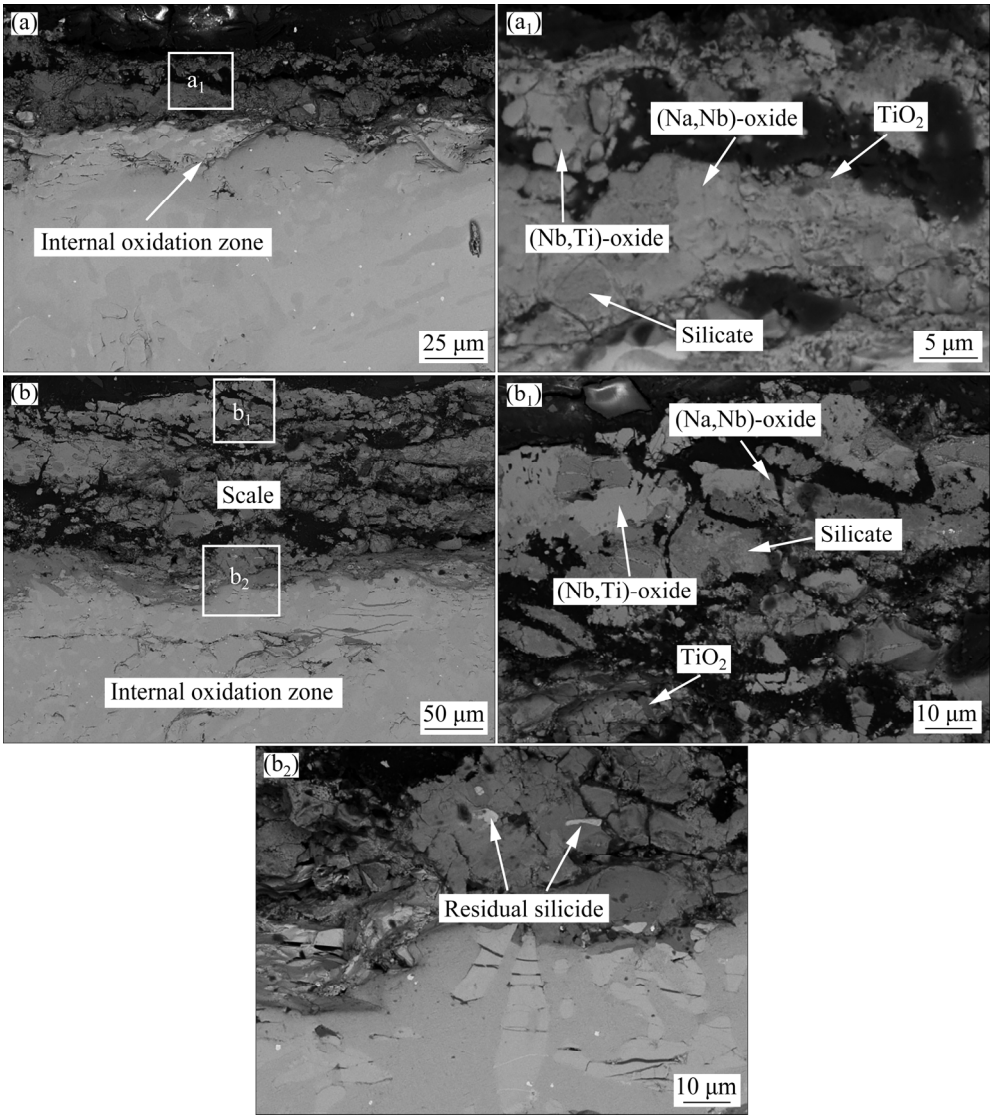

Fig. 8 Cross-sectional BSE images of Nb−Si based alloys after hot corrosion for 1 h (a, a_1) and 20 h (b, b_1, b_2)

Table 3 Chemical compositions of marked sites in Fig. 8, determined by WDS analysis

Corrosion time/h	Phase	Composition/at.%									
		Nb	Ti	Si	Cr	Al	Hf	O	S	Cl	Na
1	(Nb,Ti)-oxide	22.42	4.75	0.13	1.81	1.28	0.44	66.10	0.02	0.05	2.95
	(Na,Nb)-oxide	13.78	3.91	0.16	1.12	0.82	0.45	66.41	0.08	0.06	13.21
	Silicate	9.10	3.67	13.61	0.14	0.76	1.17	66.62	0.04	0.01	4.88
	TiO_2	0.10	30.67	0.03	0.54	1.04	0.02	65.74	0.02	0.01	1.37
20	(Nb,Ti)-oxide	24.31	3.64	0.20	1.91	1.10	0.30	66.30	0.03	0.08	2.13
	(Na,Nb)-oxide	16.12	4.05	0.21	1.01	0.89	0.21	66.27	0.12	0.04	11.08
	Silicate	9.83	3.88	14.54	0.13	0.79	1.30	65.40	0.02	0.06	4.05
	TiO_2	0.21	31.12	0.10	0.85	1.12	0.03	65.02	0.02	0.03	1.50

internal oxidation zone. Moreover, TiO_2 can be observed in the microcracks in the silicide blocks, which may be responsible for the latter rapid spallation of scale. In order to accurately obtain constituent phases of corrosion scale, the scale formed on Nb−Si based alloys after hot corrosion

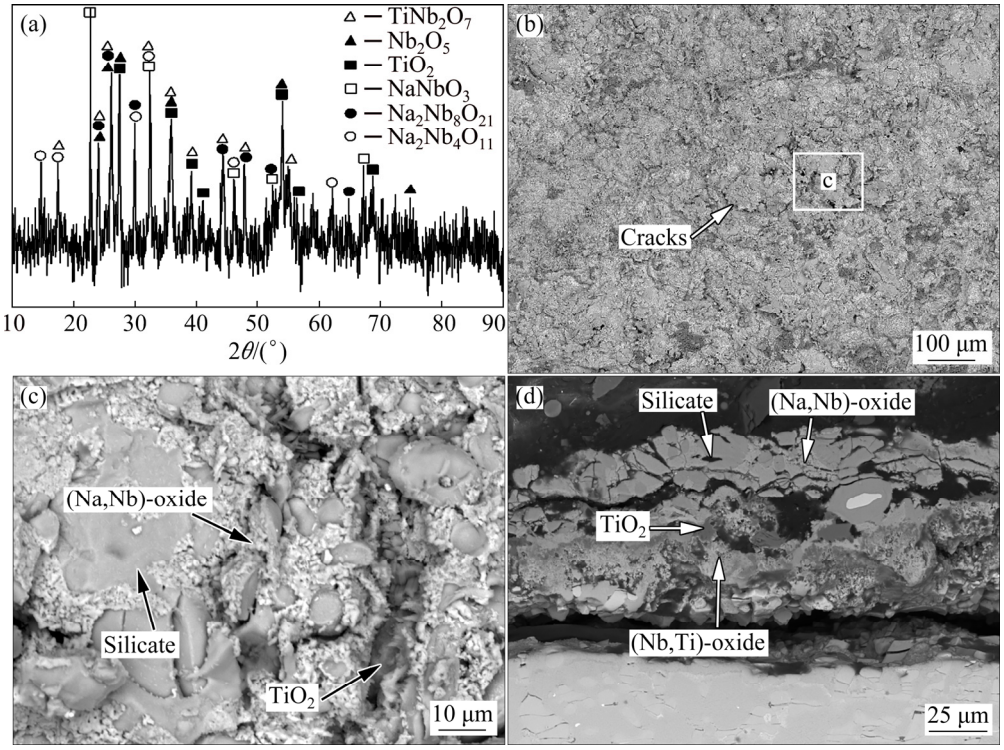

Fig. 9 XRD pattern and SEM BSE images of residual scale formed on Nb−Si based alloys after hot corrosion for 50 h: (a) XRD pattern; (b, c) Surface morphology; (d) Cross-sectional morphology

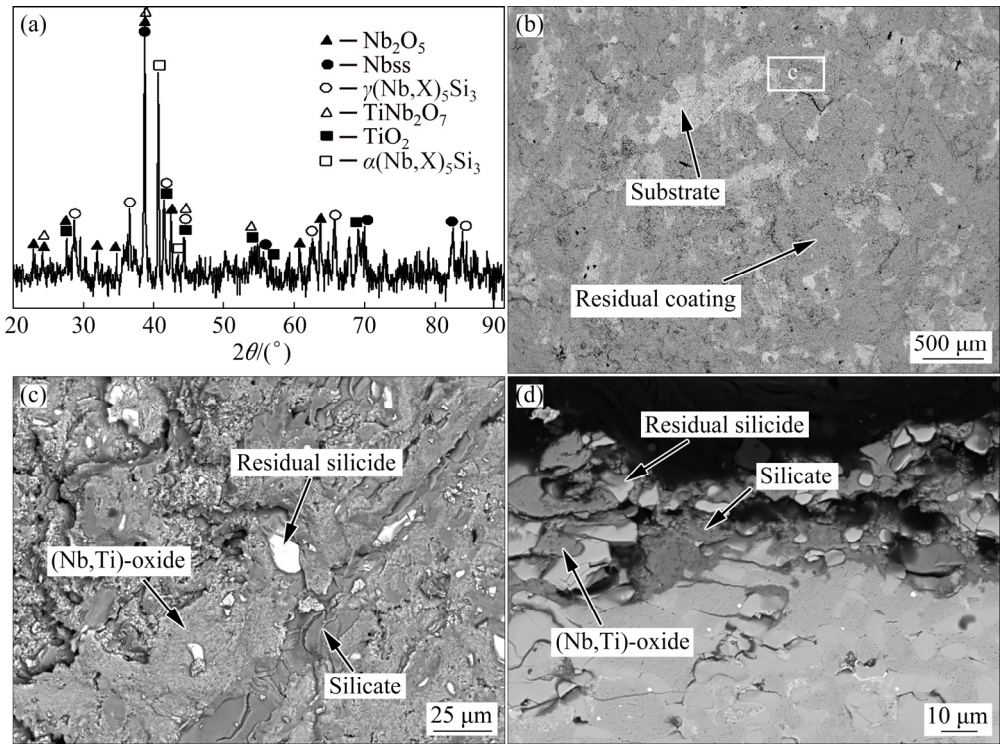

Fig. 10 XRD pattern and SEM BSE images of residual scale formed on Nb−Si based alloys after hot corrosion for 100 h: (a) XRD pattern; (b, c) Surface morphology; (d) Cross-sectional morphology

for 20 h was further analyzed by scanning/transmission electron microscope (STEM) and selected area electron diffraction (SAED), as presented in Fig. 12. The dark phase marked as A is recognized as amorphous silicate by SAED pattern and EDS mapping. The SAED pattern of Point B also

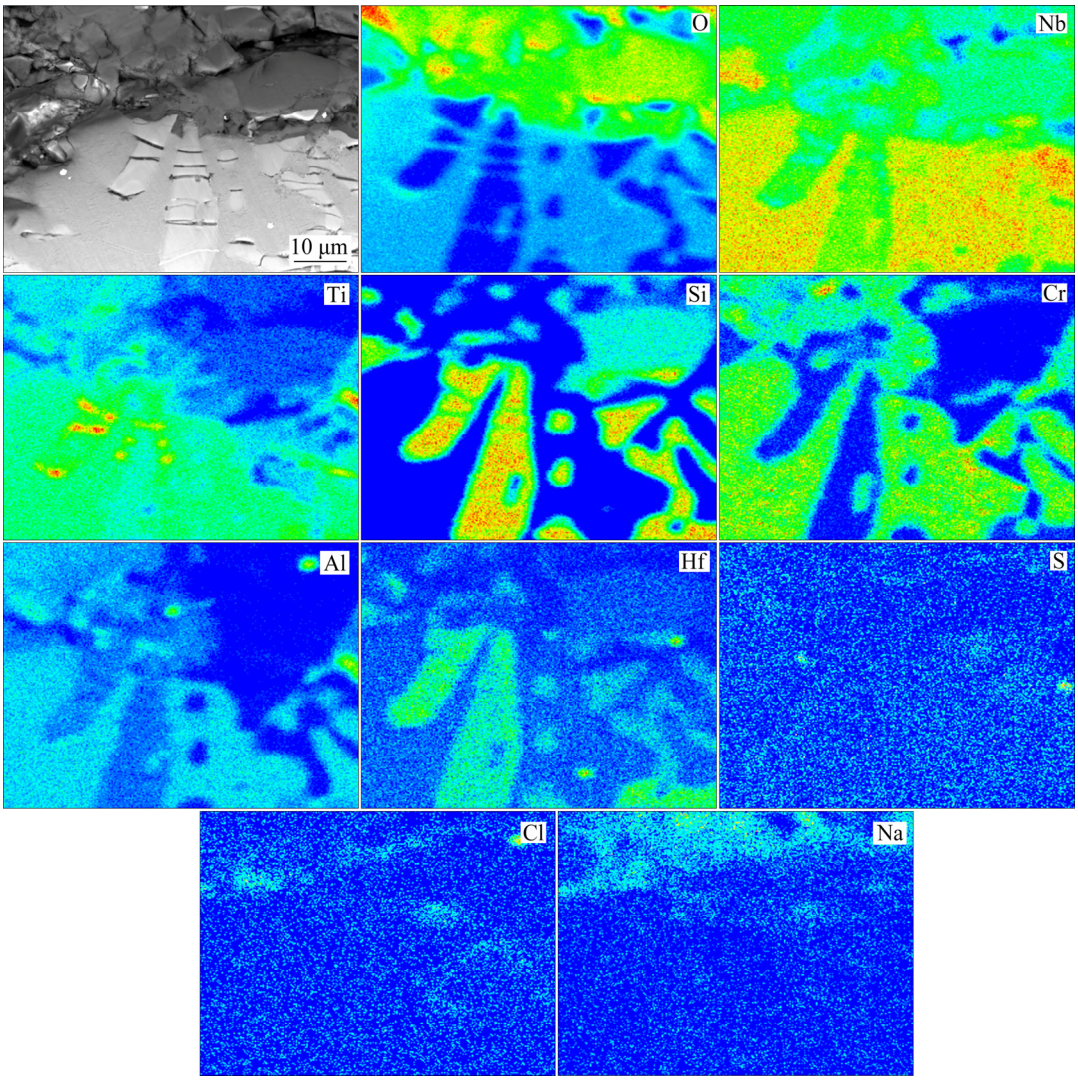

Fig. 11 Elemental mapping of internal oxidation zone of Nb−Si based alloys after hot corrosion for 20 h, determined by EPMA analysis

indicates that $NaNbO_3$ exists in the scale. Some small TiO_2 particles presented in Fig. 12(a_1) (Point C) can be confirmed by EDS mapping and SAED data. Furthermore, monoclinic $TiNb_2O_7$ and Nb_2O_5 phases labeled as D and E in Fig. 12(a_2) are also detected in the scale.

3.5 Discussion

3.5.1 Intermediate temperature oxidation

The thermogravimetry results (Fig. 2) illustrate that the mass gain of Nb−Si based alloys in air follows a parabolic kinetics during the first 50 h and then changes to linear one, suggesting that the oxidation process at 900 °C is firstly controlled by diffusion and eventually unstable process occurs. At intermediate temperature, the scale growth mainly depends on grain boundary diffusion, rather than volume diffusion owing to the higher diffusion coefficient on grain boundaries and presence of lots of grain boundaries [19]. In fact, the early stage of oxidation is controlled by the process involving adsorption, dissociation, chemisorption, and ionization of oxygen, instead of ion transportation through oxide layers. The detailed process on the alloy surface could be described by [9]

$$O_2(g)\rightarrow O_2(ad)\rightarrow 2O(ad)\rightarrow 2O^-(chem)+2h^{\cdot}\rightarrow 2O^{2-}(latt)+4h^{\cdot} \quad (1)$$

where $h^{\cdot}$ means hole.

Nevertheless, these processes are rarely observed due to their short and rapid reactions.

Once the oxidation of the alloys reaches the stage where ion diffusion is rate controlling, a parabolic kinetics law is found to hold for a period

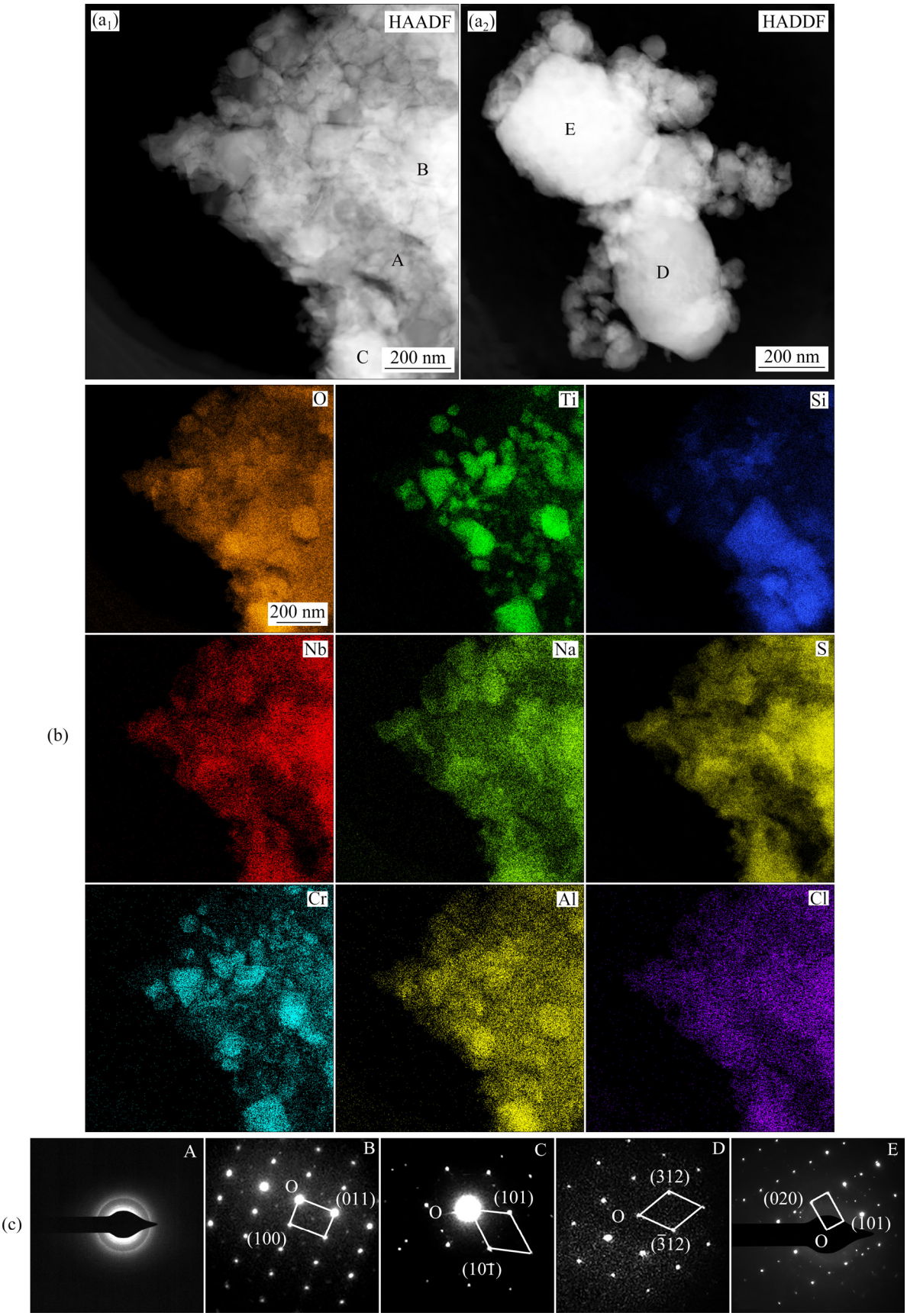

Fig. 12 STEM images of scale formed on Nb−Si based alloys after hot corrosion for 20 h: (a_1, a_2) High-angle annular dark-field images (HADDF); (b) STEM-EDS mapping; (c) SAED patterns (A—Silicate, B—$NaNbO_3$, C—TiO_2, D—$TiNb_2O_7$, and E—Nb_2O_5)

whose duration relies on some factors such as constituent phases of alloys, scale integrality and oxidation temperature. Nb−Si based alloys primarily contain oxygen-sensitive Nbss and brittle silicide. Many oxygen ions could diffuse into the matrix where it saturates in Nbss and reacts with the metals. Besides, some fine oxides (TiO_2, Al_2O_3, Cr_2O_3, etc) generate in the Nbss matrix (Fig. 5(c_3)), which will not only increase the number of grain boundary but also induce a volume expansion, eventually leading to the generation of cracks in the silicides of internal oxidation zone (Figs. 5(a, b, c_2)). MATHIEU et al [16] reported that approximately 15% volume expansion of Nbss occurs at 815 °C in air, promoting crack initiation, propagation and ruptures within silicides finally [16]. These cracks, which provide more sites for rapid oxygen ingress, growth of voluminous oxides and stress risers, are responsible for the latter linear rapid and catastrophic oxidation process, i.e., pest oxidation.

Scale integrality is another significant factor that determines the oxidation resistance of alloys. Thus, internal stress generation and relief in the scale, if stress-induced cracking or spallation may occur, should be considered during oxidation process. As is well known, the internal stress could be divided into growth stress, which develops during the isothermal oxidation process, and thermal stress arising from differential thermal expansion between substrate and scale [9]. The growth stress is closely related to the PBR (Pilling−Bedworth ratio) of oxides as well as new oxides formed within the scale. The PBRs of TiO_2 (1.78) and Nb_2O_5 (2.68) [9,19] are far greater than one, indicating that large compressive stress occurs in the scale during the growth of these oxides, then inducing scale cracking (Figs. 4 and 5), even partial spallation. Besides, since inward migration of oxygen along oxide grain boundaries is dominant at intermediate temperature, new oxides formed within the scale could also lead to compressive stress in the scale. For the thermal stress, the difference in thermal expansion coefficient (CTE) of the alloy and oxides is more important. The CTEs of related oxides and Nb−Si based alloys are respectively as follows: TiO_2 (8.2×10^{-6} K^{-1}) [20], Nb_2O_5 ($(1.07-2.24)\times10^{-6}K^{-1}$) [21] and Nb−Si based alloys ($10.45\times10^{-6}K^{-1}$) [22]. The stress induced by thermal expansion mismatch could be evaluated in the following equation [23]:

$$\sigma=E_o/(1-v_o)\cdot\Delta\alpha\Delta T \quad (2)$$

where E_o and v_o are the elastic modulus and Possion ratio of the oxide scale, respectively; $\Delta\alpha$ represents the difference between the CTEs of the scale and substrate; ΔT represents the temperature variation. Therefore, large compressive stress will develop in the scale during cooling due to the thermal expansion mismatch between oxide (Nb_2O_5) and substrate alloy. Once these stresses release, severe scale cracking, even pulverization will occur, as shown in Figs. 2, 4 and 5.

Besides, at intermediate temperature, numerous oxygen ions ingress along grain-boundaries could result in grain-boundary hardening, and then induce the later pest degradation. WESTBROOK and WOOD [24] have proposed a pest degradation model, based on grain-boundary hardening measurement. According to this model, at some intermediate temperature, oxygen diffuses rapidly through the alloy along grain-boundary paths. At the initial stage, oxygen is confined at the grain-boundaries, and then embrittles them. At the later rapid oxidation stage, lots of fine oxides formed at the grain-boundaries, promote internal stresses arising and fragment the alloy along the grain-boundaries, eventually inducing the scale pulverization.

Based on the macrographic morphologies, microstructural observation and above discussion, the later linear oxidation stage (i.e. pest oxidation) of the alloy is related with volume expansion of Nbss, large internal stress generation as well as numerous oxides formed at grain-boundaries.

3.5.2 Hot corrosion

The intrinsic form of hot corrosion is an accelerated oxidation, which occurs when the air is contaminated with impurities (such as Na_2SO_4, K_2SO_4, NaCl and KCl). In this work, Na_2SO_4 and NaCl molten salts are selected as corrosive medium to investigate the hot corrosion behavior of Nb−Si based alloys. Since the melting point of the mixture of Na_2SO_4 and NaCl is lowered to about 620 °C, the salt mixture would be in a molten state at 900 °C [8]. During the hot corrosion process, the molten salts are adherent on the surface of Nb−Si based alloys. Meanwhile, some specific reactions occur firstly at the molten salt/metal interface as follows [12−14]:

$$Na_2SO_4\rightarrow Na_2O+SO_3 \quad (3)$$

$$Na_2SO_4 \rightarrow Na_2O+SO_2+1/2O_2 \quad (4)$$

$$Na_2SO_4 \rightarrow Na_2O+S+3/2O_2 \quad (5)$$

$$2NaCl+SO_2+O_2 \rightarrow Na_2SO_4+Cl_2 \quad (6)$$

$$2NaCl+SO_3+1/2O_2 \rightarrow Na_2SO_4+Cl_2 \quad (7)$$

Once the surface of the alloy has been partially or completely wetted by the molten salts, conditions for serious corrosion may develop. As is well known, the hot corrosion process of virtually all susceptible alloys involves two stages: an initial stage during which the corrosion rate is slow, and similar to that in the absence of the contamination, and a propagation stage in which rapid, even catastrophic, corrosion occurs [9,25]. According to the hot corrosion kinetics curves, macrographic morphologies and microstructural observation of the corroded alloy (Figs. 2, 7, 8, 9 and 10), it can be seen that the hot corrosion process could be divided into two stages: an initial parabolic stage and a propagation linear stage, as summarized diagrammatically in Fig. 13(a). Step t0 gives the stable microstructure of the alloy before hot corrosion, mainly consisting of Nbss matrix and silicide blocks (the morphology difference between $\alpha(Nb,X)_5Si_3$ and $\gamma(Nb,X)_5Si_3$ is negligible during the hot corrosion process). At the initial stage, elements (Nb, Ti, Si, Cr, Al, etc) in the alloy are oxidized by oxygen from the salts and gas environment. Consequently, the reaction products that are formed beneath the salts on the alloy surface exhibit characteristics similar to those in the absence of the salts [9]. For example, an internal oxidation zone which is featured by cracked silicide and saturated (oxygen) Nbss matrix is formed in the corroded alloy and oxidized alloy (Figs. 5(a), 8(a) and Step t1). Due to the evaporation of SO_3, SO_2, Cl_2 and O_2 via Reactions (3)−(7), the surplus Na_2O offers an alkaline environment at the salts/scale interface. Subsequently, the main formed oxides (Nb_2O_5, TiO_2, etc) are dissolved into the salts via the Reactions (8) and (9). When it comes to the reactions between Si-containing oxides and Na_2O,

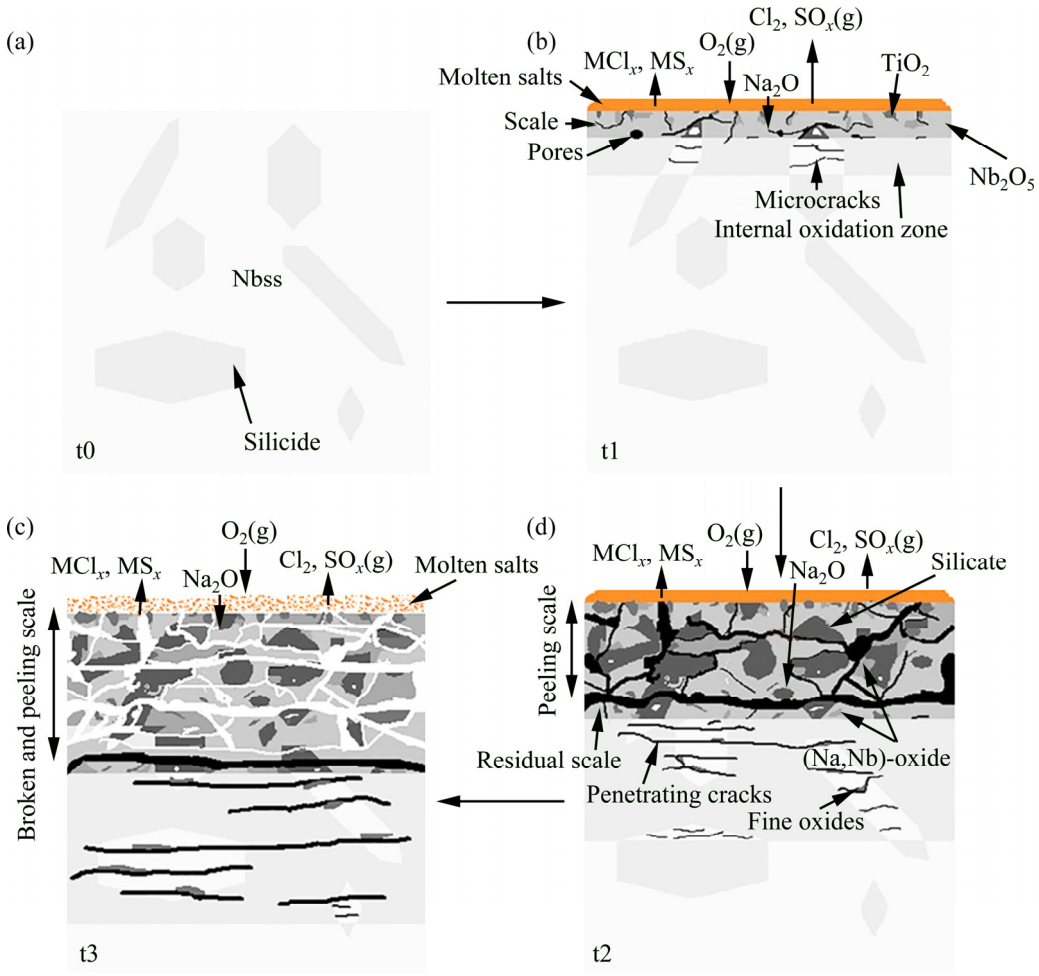

Fig. 13 Schematic illustration of hot corrosion process of Nb−Si based alloys at 900 °C

the corrosion products could be amorphous silicate via Reaction (10) [26]:

$$Nb_2O_5+Na_2O\rightarrow 2NaNbO_3 \quad (8)$$

$$TiO_2+Na_2O\rightarrow Na_2TiO_3 \quad (9)$$

$$mSiO_2+Na_2O\rightarrow Na_2O\cdot mSiO_2 \quad (10)$$

$$2Nb_2O_5+Na_2O\rightarrow Na_2Nb_4O_{11} \quad (11)$$

$$4Nb_2O_5+Na_2O\rightarrow Na_2Nb_8O_{21} \quad (12)$$

Moreover, $Na_2Nb_4O_{11}$ and $Na_2Nb_8O_{21}$ are also found in the corroded scale for long time, especially in the scale of 50 h (Figs. 6 and 9). This means that sodium salts gradually intrude into the lower part of scale and react with numerous new Nb_2O_5 products during the later rapid corrosion stage (Step t2), via Reactions (11) and (12).

In addition, the corrosive media like Cl_2, SO_2 and SO_3, even the molten salts, may permeate into the alloy along some cracks or pores. Considering that the oxygen attack continuously occurs during the whole hot corrosion process, an oxychlorination reaction could occur via Reactions (13) and (14) (M=Nb, Ti, Cr, etc) [14,27]:

$$xM+y/2O_2+zNaCl\rightarrow Na_zM_xO_y+z/2Cl_2 \quad (13)$$

$$xMO+y/2O_2+zNaCl\rightarrow Na_zM_xO_{y+x}+z/2Cl_2 \quad (14)$$

Moreover, sulphidation reactions are unavoidable because of the close relationship between sulphidation and basic fluxing in the hot corrosion process [9]. At high temperatures (> 850 °C) and in lower SO_3 or SO_2 pressures, basic fluxing occurs due to sulphur removal from the Na_2SO_4 into the alloy. Consequently, since the alloy suffers hot corrosion attack via basic fluxing, the hot corrosion process may gradually change to sulphidation as a result of the fairly high number of sulphur intruding into the alloy [9]. More than detrimental effects of sulphur, chlorine can significantly accelerate the damage of protective oxides due to the self-maintenance of chlorination reactions [28,29]. Thus, these sulphidation and chlorination reactions could be expressed by the Reactions (15) and (16). And the relevant standard Gibbs free energy changes ($\Delta G^{\ominus}$) as a function of temperature (per mol O_2, Cl_2 or S_2) are presented in Fig. 14. From 600 to 1000 °C, the standard Gibbs free energy changes of forming sulfides and chlorides are negative and lower than those of corresponding oxides, indicating that these oxides

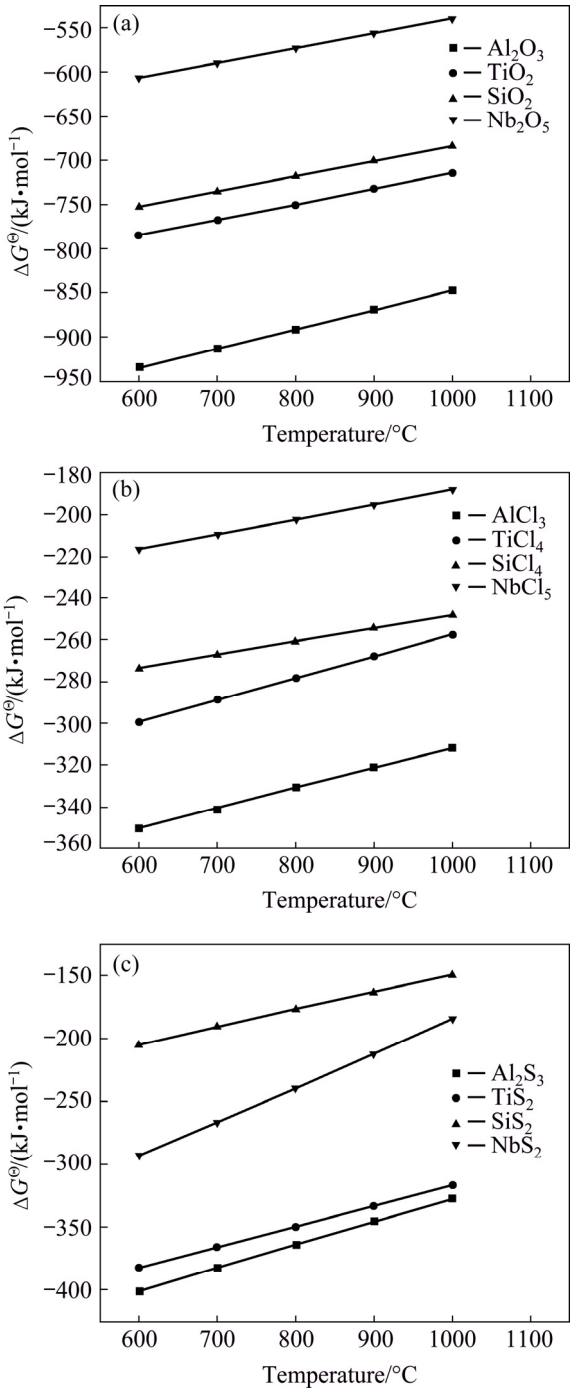

Fig. 14 Standard Gibbs free energy changes ($\Delta G^{\ominus}$) of main oxides, sulfides and chlorides as function of temperature (per mol O_2 (a), Cl_2 (b) or S_2 (c))

are thermodynamically more stable than sulfides and chlorides. GRABKE et al [30] have designed a flow apparatus combined with a thermobalance to perform in-situ corrosion and found the existence of $FeCl_2$ (g) at the oxide/metal interface during hot corrosion process of steels. As a consequence, these as-formed volatile sulfides and chlorides [31], with

low boiling points ($NbCl_5$ (254 °C), $TiCl_4$ (135.9 °C), $AlCl_3$ (178 °C) and $SiCl_4$ (57.6 °C)) and high vapor pressures, volatilize outward, or react with O_2 or O ions at the region with higher partial oxygen pressure to form non-protective oxides, and release Cl_2 and S_2, SO_3 or SO_2 via Reactions (17)−(20). Once these processes develop, the scale could be easily destroyed with large amounts of cracks, voids and holes, leaving more paths for rapid infiltration of corrosive media. Meanwhile, these as-generated Cl_2 and S_2, SO_3 or SO_2 would further destroy the scale and accelerate the oxidation of the alloy, eventually leading to the formation of a broken and peeling scale (Step t3).

$$M+x/2S_2(g)\rightarrow MS_x \quad (15)$$

$$M+y/2Cl_2(g)\rightarrow MCl_y \quad (16)$$

$$2MS_x+O_2\rightarrow 2MO+xS_2 \quad (17)$$

$$MS_x+(x+1/2)O_2\rightarrow MO+xSO_2 \quad (18)$$

$$MS_x+(3x+1)/2O_2\rightarrow MO+xSO_3 \quad (19)$$

$$2MCl_y+O_2\rightarrow 2MO+yCl_2 \quad (20)$$

Also, the self-maintenance of sulphidation and chlorination reactions could be further explained by the criterion for a self-maintaining fluxing hot corrosion process [32]:

$$\left(\frac{dS_o}{dL}\right)_{L=0}>0 \quad (21)$$

where S_o is the oxide solubility and L is the distance from the salt/oxide interface in the molten salt. The criterion indicates that the oxide will dissolve at the salt/scale interface (L=0) and reprecipitate away from the gas/salt interface (where the solubility is lower and oxygen partial pressure is higher) as non-protective oxides.

4 Conclusions

(1) Thermogravimetry results indicate that both oxidation and hot corrosion processes at 900 °C of Nb−Si based ultrahigh temperature alloys could be divided into two main stages: an initial parabolic stage and a rapid linear stage.

(2) At 900 °C in static air, a very thin, dense and continuous scale is formed on the alloy for 1−50 h, while a powder-like and loose scale with a thickness of approximately 650 μm is observed after oxidation for 100 h.

(3) The corroded scale is mainly composed of TiO_2, Nb_2O_5, $TiNb_2O_7$, amorphous silicate and $NaNbO_3$. Compared with oxidation of the alloy, a linear corrosion stage occurs earlier (over 20 h) and severely catastrophic scale disintegration occurs after hot corrosion for 20−100 h, indicating that the molten salts (Na_2SO_4 + NaCl) could severely undermine Nb−Si based alloys.

Acknowledgments

The authors are grateful for the financial supports from the National Natural Science Foundation of China (51971181, 51971177), and the National Key R&D Program of China (2017YFB0702903).

References

[1] WANG Jia-yi, JIA Li-na, MA Li-min, YUAN Sai-nan, ZHANG Xiao-li, ZHANG Hu. Microstructure optimization of directionally solidified hypereutectic Nb−Si alloy [J]. Transactions of Nonferrous Metals Society of China, 2013, 23: 2874−2881.

[2] GUO Hai-sheng, GUO Xi-ping. Microstructure and microhardness of directionally solidified and heat-treated Nb−Ti−Si based ultrahigh temperature alloy [J]. Transactions of Nonferrous Metals Society of China, 2011, 21: 1283−1290.

[3] GENG J, TSAKIROPOULOS P. A study of the microstructure and oxidation of Nb−Si−Cr−Al−Mo in situ composites alloyed with Ti, Hf and Sn [J]. Intermetallics, 2007, 15: 382−395.

[4] ZHANG Song, GUO Xi-ping. Microstructure, mechanical properties and oxidation resistance of Nb silicide based ultrahigh temperature alloys with Hf addition [J]. Materials Science and Engineering A, 2015, 645: 88−98.

[5] TANG Ye, GUO Xi-ping. Flow behavior and hot workability of Nb−15Si−22Ti−5Cr−3Al−2.5Hf alloy [J]. Metallurgical and Materials Transactions A, 2018, 49: 4884−4894.

[6] HUANG Yong-lin, JIA Li-na, JIN Zu-heng, KONG Bin, GUO Yue-ling, SHA Jiang-bo, ZHANG Hu. Effect of Sc on the microstructure and room-temperature mechanical properties of Nb−Si based alloys [J]. Materials & Design, 2018, 160: 671−682.

[7] GUO Hai-sheng, GUO Xi-ping. Microstructure evolution and room temperature fracture toughness of an integrally directionally solidified Nb−Ti−Si based ultrahigh temperature alloy [J]. Scripta Materialia, 2011, 64: 637−640.

[8] ELIAZ N, SHEMESH G, LATANISION R M. Hot corrosion in gas turbine components [J]. Engineering Failure Analysis, 2002, 9: 31−43.

[9] BIRKS N, MEIER G H, PETTIT F S. Introduction to the high-temperature oxidation of metals [M]. 2nd ed. New York: Cambridge University Press, 2006.

[10] HANCONCK P. Vanadic and chloride attack of superalloys [J]. Material Science and Technology, 1987, 3: 536−544.

[11] QIAN Yu-hai, LI Xi-chao, LI Mei-shuan, XU Jing-jun, LU Bin. Hot corrosion of modified Ti_3Al-based alloy coated with thin Na_2SO_4 film at 910 and 950 °C in air [J].

Transactions of Nonferrous Metals Society of China, 2017, 27: 954−961.
[12] GREGOIRE B, MONTERO X, GALRTZ M C, BONNET G. PEDRAZA F. Mechanisms of hot corrosion of pure nickel at 700 °C: Influence of testing conditions [J]. Corrosion Science, 2018, 141: 211−220.
[13] YUWEN Pei, ZHOU Chun-gen. Improved hot corrosion resistance of Dy−Co-modified aluminide coating by pack cementation process on nickel base superalloys [J]. Corrosion Science, 2016, 112: 710−717.
[14] QIAO Yan-qiang, KONG Jian-ping, GUO Xi-ping. Hot corrosion phenomena of Nb−Ti−Si based alloy and its silicide coating induced by different corrosive environments at 900 °C [J]. Ceramics International, 2018, 44: 7978−7990.
[15] ZELENITSAS K, TSAKIROPOULOS P. Effect of Al, Cr, Ta additions on the oxidation behaviour of Nb−Ti−Si in situ composites at 800 °C [J]. Materials Science and Engineering A, 2016, 416: 269−280.
[16] MATHIEU S, KNITTLE S, BERTHOD P, MATHIEU S, VILASI M. On the oxidation mechanism of niobium-base in situ composites [J]. Corrosion Science, 2012, 60: 181−192.
[17] HE Jia-hua, GUO Xi-ping, QIAO Yan-qiang. Microstructure evolution and hot corrosion behavior of Zr−Y modified silicide coating prepared by two-step process [J]. Corrosion Science, 2019, 156: 44−57.
[18] LEFEZ B, JOUEN S, HANNOYER B, BACOS M P, BEUCHER E. Oxidation behaviour of the 47Nb−16Si−25Ti−8Hf−2Al−2Cr alloy sheet and vibrational spectroscopy [J]. Materials at High Temperature, 2009, 26: 15−20.
[19] LI M S. High temperature corrosion of metal [M]. Beijing: Metallurgy Industry Press, 2001. (in Chinese)
[20] JIANG Shao-song, ZHANG Kai-feng. Study on controlling thermal expansion coefficient of ZrO_2−TiO_2 ceramic die for superplastic blow-forming high accuracy Ti−6Al−4V component [J]. Materials & Design, 2009, 30: 3904−3907.
[21] DOUGLASS D L. The thermal expansion of niobium pentoxide and its effect on the spalling of niobium oxidation films [J]. Journal of the Less-Common Metals, 1963, 5: 151−157.
[22] BEWLAY B P, JACKSON M R, LIPSITT H A. The balance of mechanical and environmental properties of a multielement niobium silicide-based in situ composite [J]. Metallurgical and Materials Transactions A, 1996, 27: 3801−3808.
[23] CHRISTENSEN R J, TOLPYGO V K, CLARKE D R. The influence of the reactive element yttrium on the stress in alumina scales formed by oxidation [J]. Acta Materialia, 1997, 45: 1761−1766.
[24] WESTBROOK J H, WOOD D L. “Pest” degradation in beryllides, silicides, aluminides, and related compounds [J]. Journal of Nuclear Materials, 1964, 2: 208−215.
[25] STRINGER J. High-temperature corrosion of superalloys [J]. Materials Science and Technology, 1987, 3: 482−493.
[26] GE Yu-lin, WANG Ya-ming, CHEN Jun-chen, ZOU Yong-chun, GUO Li-xin, OUYANG Jia-hu, JIA De-chang, ZHOU Yu. Hot corrosion behavior of $NbSi_2$/SiO_2−Na_2O_5 multilayer coating on Nb alloy [J]. Journal of Alloys and Compounds, 2018, 767: 7−15.
[27] TSAUR C C, ROCK J C, CHANG Y Y. The effect of NaCl deposit and thermal cycle on an aluminide layer coated on 310 stainless steel [J]. Materials Chemistry and Physics, 2005, 91: 330−337.
[28] BAO Ze-bin, WNAG Qi-min, LI Wei-zhou, LIU Xu, GONG Jun, XIONG Tian-ying, SUN Chao. Preparation and hot corrosion behaviour of an Al-gradient NiCoCrAlYSiB coating on a Ni-base superalloy [J]. Corrosion Science, 2009, 51: 860−867.
[29] SHINATA Y. Accelerated oxidation rate of chromium induced by sodium−chloride [J]. Oxidation of Metals, 1987, 27: 315−332.
[30] GRABKE H J, REESE E, SPIEGEL M. The Effects of chlorides, hydrogen chloride, and sulfur dioxide in the oxidation of steels below deposits [J]. Corrosion Science, 1995, 37: 1023−1043.
[31] DAI Jing-jie, ZHANG Hong-xia, SUN Cai-xia, LI Shou-ying, CHEN Chuan-zhong, YANG Yong. The effect of Nb and Si on the hot corrosion behaviors of TiAl coatings on a Ti−6Al−4V alloy [J]. Corrosion Science, 2020, 168: 108578.
[32] RAPP R A, GOTO K S. Corrosion in fused salts [M]. BRAUNSTEIN J, SELMAN J R, Ed. Princeton, New Jersey: The Electrochemical Society, 1981: 159.

Nb−Si 基超高温合金在 900 °C 下的氧化和热腐蚀行为

何佳华，郭喜平，乔彦强

西北工业大学 凝固技术国家重点实验室，西安 710072

摘　要：对 Nb−Si 基超高温合金在 900 °C 下的氧化和热腐蚀行为进行研究。结果表明：合金的氧化和热腐蚀动力学均由初始的抛物线增长阶段和随后的线性快速增长阶段组成。在氧化的初始阶段(1~50 h)，合金表面形成较薄且连续的氧化膜，而在随后的线性阶段，合金表面发生严重的“粉化”现象。合金经热腐蚀后，其线性增长阶段发生得更早，同时在热腐蚀 20~100 h 后发生灾难性的氧化膜剥落现象，表明熔盐(Na_2SO_4 和 NaCl)能显著加快合金的氧化过程。STEM 结果显示，热腐蚀后的氧化膜主要由 TiO_2、Nb_2O_5、$TiNb_2O_7$、非晶硅酸盐和 $NaNbO_3$ 组成。

关键词：Nb−Si 基合金；熔盐；氧化；热腐蚀；硅酸盐

(Edited by Bing YANG)